Graphene oxide chemically reduced and functionalized with KOH-PEI for efficient Cr(VI) adsorption and reduction in acidic medium

Yasmine Tadjenant, Nahed Dokhan, Alexandre Barras, Ahmed Addad, Roxana Jijie, Sabine Szunerits, Rabah Boukherroub

Graphene oxide chemically reduced and functionalized with KOH-PEI for efficient Cr(VI) adsorption and reduction in acidic medium

Yasmine Tadjenant,[1,2] Nahed Dokhan,[2] Alexandre Barras,[1] Ahmed Addad,[3] Roxana Jijie,[1] Sabine Szunerits[1] and Rabah Boukherroub[1]*

[1] *Univ. Lille, CNRS, Centrale Lille, Univ. Polytechnique Hauts-de-France, UMR 8520 - IEMN, F-59000 Lille, France*

[2] *Research Unit, Materials, Processes and Environment (URMPE), University of Boumerdes, Algeria*

[3] *Univ. Lille, CNRS, UMR 8207 – UMET, F-59000 Lille, France*

*To whom correspondence should be addressed: Rabah Boukherroub (rabah.boukherroub@univ-lille.fr; Tel: +333 62 53 17 24)

Abstract

In this study, graphene oxide (GO), polyethyleneimine (PEI) and potassium hydroxide (KOH) were used to synthesize reduced graphene oxide (rGO/PEI-KOH) nanocomposite. The presence and grafting of PEI molecules on the reduced GO surface were assessed by X-ray photoelectron spectroscopy (XPS) and Fourier transform infrared (FTIR) analyses. The rGO/PEI-KOH nanocomposite was successfully applied for hexavalent chromium, Cr(VI), wastewater elimination. The resulting rGO/PEI-KOH adsorbent was found to be highly effective for Cr(VI) removal at low pH values and achieved a maximum capacity of experimental adsorption of 398.9 mg/g, which is one of the highest sorption capacity of most GO- and PEI-based adsorbents reported in the literature up to date. Studying the adsorption mechanism, the sorption isotherm revealed that the modified-Langmuir model was the best fit and Cr(VI) removal follows a pseudo-second-order kinetics, with the predominance of intraparticle diffusion during the first step of adsorption. XPS analysis indicated the presence of appreciable amount of Cr(III) on the adsorbent surface, which suggests that the adsorbed Cr(VI) ions were effectively reduced to Cr(III) on the rGO/PEI-KOH adsorbent surface (~70% of the total adsorbed Cr). Cr(VI) adsorption and subsequent reduction to Cr(III) both contributed to the Cr(VI) removal. The results of the present study highlight the benefits of rGO/PEI-KOH like low cost, environmentally friendly, large toxic Cr(VI) ions adsorption capacity and its effective reduction to less-toxic Cr(III).

Keywords: *Reduced graphene oxide; Polyethylenimine; Cr(VI) adsorption; High adsorption capacity; Cr(VI) reduction.*

1. Introduction

Chromium is one of the most toxic heavy metals discharged into the environment and constitutes one of the main causes of environmental pollution associated with a non-negligible health problem. It commonly originates from diverse industrial wastewaters, derived from factories of electroplating, tanning, textile dyeing, stainless steel production, water cooling, and other industries (Barnhart, 1997).

Chromium is usually found in trivalent (III) as well as hexavalent (VI) states. While Cr(VI) is highly toxic and can lead to severe illnesses such as dermatitis, kidney failure, lung cancer and even death, Cr(III) is less toxic and represents an important element for the proper functioning of living organisms (Zhou et al., 2016). Therefore, Cr(VI) is viewed as a critical polluting agent and is listed by the US Environmental Protection Agency as class A human carcinogen (US-EPA1998). Hence, eliminating Cr(VI) from wastewater or reducing it to Cr(III) prior to discharge into the environment is imperative.

Several methods have been developed for the removal of Cr(VI) from aqueous media, including physical (washing or electrical enrichment), biological (plant enrichment), and chemical (adsorption and reduction) approaches. However, most of these methods and particularly the physical and biological processes experience several limitations such as complexity of operation and elevated costs, and require long periods of time, which has significantly impeded their use in Cr(VI) treatment. In contrary, the chemical method is a favored technique because of its flexibility, high efficiency, design and operational simplicity for the elimination of Cr(VI) and thus it is attracting increasing attention (Zhou et al., 2016; Wang et al., 2017).

In chemical methods, various adsorbents have been identified to withdraw Cr(VI) from polluted water, such as activated carbon (Sandhya and Tonni, 2004), KOH-modified carbonized eucalyptus sawdust (Zhang et al., 2018a), PEI-modified biomass (Deng and Ting,

2005), mesoporous carbon microspheres (Zhou et al., 2016), iron nanoparticle-decorated graphene (Jabeen et al., 2011), etc. However, biosorbents have often low surface area and limited mechanical resistance, causing additional potential secondary emissions in extreme conditions. On the other hand, bare metallic nanoparticles are readily oxidizable and can easily agglomerate, while carbon-based adsorbents display a relatively low adsorption capacity. Such forms of disadvantages have impeded their use for Cr(VI) elimination from wastewater (Ma et al., 2012; Zhang et al., 2018b). Therefore, the development of new materials with a large surface area, high removal efficiency, stability in extreme conditions and easy separation procedure is very attractive.

Most recently, chemical methods for the synthesis of adsorbents exhibiting high performance for simultaneous adsorption and reduction of Cr(VI) turns to an applicable research hotspot (Ma et al., 2012; Wang et al., 2017; Zhang et al., 2018b). Graphene oxide (GO), consisting of a monolayer of carbon atoms covalently bonded, forms one of the currently most investigated two-dimensional nanomaterial. GO displays an ultra large active surface area and plentiful of oxygen containing functional groups (e.g., -OH, -C=O, -COOH). Reduced GO (rGO), obtained from GO reduction using different means, has been investigated as an efficient adsorbent for Cr(VI) thanks to its high capacity of adsorption (He et al., 2017; Pakulski et al., 2018).

KOH reduction of GO was firstly reported by Fan et al. (Fan et al., 2008) who noticed that a chemically stable suspension of graphene can be easily prepared by a simple heating of exfoliated graphite oxide at mild temperatures (50-90°C) in strongly alkaline conditions. But no noticeable works has been reported on the Cr(VI) adsorption/reduction by GO treated with KOH.

Polyethyleneimine (PEI) with plenty of primary and secondary amine groups present in a macromolecular chain can partially reduce and simultaneously functionalize GO (Shao et al.,

2016). PEI-functionalized GO exhibits interesting adsorption ability for removing toxic cations (Pakulski et al., 2018).

Compared with chemical reduction using strong and toxic agents like hydrazine and sodium borohydride, chemical reduction with KOH or PEI is less efficient for completely eliminating the oxygen-containing functional groups on GO, but they have the advantage of being environmentally friendly. Additionally, their simultaneous use may be interesting as in chemical reduction processes of GO, elimination of oxygen groups is generally selective depending on the reducing reagent used (Hayes et al., 2014; Nia et al., 2017). Hence, combining two soft reducing chemicals may represent an efficient manner to optimize deoxygenation of GO sheets, while simultaneously functionalizing the resulting rGO.

In the present work, a strong KOH solution containing PEI as a reducing and functionalizing agent is proposed to prepare a nanocomposite material, rGO/PEI-KOH, under mild reaction conditions. The resulting rGO/PEI-KOH was investigated for Cr(VI) elimination. The rGO/PEI-KOH not only exhibited high adsorption capacity, but it was able to effectively reduce the adsorbed Cr(VI) to low toxic Cr(III) ions.

2. Experimental

2.1. Materials

Polyethylenimine (PEI, MW~25,000), potassium hydroxide (KOH), potassium dichromate ($K_2Cr_2O_7$), and hydrogen chloride (HCl) were purchased from Sigma-Aldrich. Graphene oxide (GO) powder was obtained from Graphenea-Spain. Milli-Q water (resistivity: 18.2 MΩ.cm) was utilized throughout this work.

2.2. Preparation of rGO/PEI-KOH nanocomposite

An easy preparation technique of rGO/PEI-KOH was established in this work. In short, 20 mg of GO was added to 18 mL of water and sonicated for 1 h to form a homogeneous solution.

Then, 2 mL of PEI aqueous solution (1 mg/mL) was added. The resulting suspension was mixed under vigorous stirring for 5 h at room temperature. Thereafter, 40 mg of KOH was added to the mixture and stirred at 90°C for 24 h. The color of the dispersion changed from yellow-brown to black, signifying the transformation of GO to reduced graphene oxide (rGO). The obtained black precipitate was isolated by centrifugation (4600 rpm) and washed copiously with water and ethanol to remove excess of PEI and KOH. Finally, the rGO/PEI-KOH was obtained and dried at 80°C for overnight (**Scheme 1**).

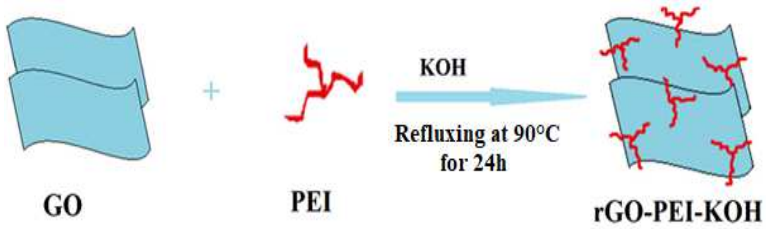

Scheme 1. Schematic illustration of rGO/PEI-KOH preparation.

2.3. Cr(VI) removal experiments

A stock solution of Cr(VI) (20 mg/mL) was obtained by dissolving $K_2Cr_2O_7$ in Milli-Q water. The stock solution was diluted to prepare different concentrations. We varied the initial concentration of Cr(VI) from 50 to 700 mg/L, the pH from 2 to 9, the dosage of adsorbent from 0.5 to 2.5 mg/mL, and the contact time from 10 to 1440 min. 0.1 M HCl or 0.1 M NaOH aqueous solution was used to adjust the pH value. All adsorption experiments were performed at ambient temperature. Adsorption experiments were performed by adding 2 mg of rGO/PEI-KOH into 2 mL of Cr(VI) aqueous solution. After being shaken for 24 h, the solution was subjected to centrifugation at 13,500 rpm during 5 min and finally UV-vis spectrophotometry was used to determine the residual concentration of Cr(VI) in the supernatant at the maximum absorption wavelength of 348 nm in acidic pH and at 372 nm in alkaline pH.

147 The effect of initial Cr(VI) amount, pH, and contact time on the efficiency of Cr(VI)
148 elimination was investigated. Afterwards, the percentage of removal R (%) and the capacity
149 of adsorption (Qe, mg/g) of Cr(VI) were calculated using equations (1) and (2), respectively:

150 $$R(\%) = \left(\frac{C_0 - C_e}{C_0}\right) \times 100 \quad (1)$$

151 $$Q_e = (C_0 - C_e)V/M \quad (2)$$

152 Where C_0 (mg/L) is the initial concentration of Cr(VI) ions, C_e (mg/L) is the equilibrium
153 concentration of Cr(VI) ions, Qe (mg/g) is the capacity of adsorption, V(L) is the initial
154 volume of Cr(VI) solution, and M (g) is the mass of the as-elaborated rGO/PEI-KOH.

155

156 ## 3. Results and discussion

157 ### 3.1. Morphological and chemical analysis

158 **Figure 1** depicts the SEM images of rGO/PEI-KOH at different magnifications. It reveals
159 wrinkled flakes aspect of thin and random rGO/PEI-KOH sheets; the nanosheets are visibly
160 crumpled in an agglomerated phase. The presence of these many wrinkles is most likely due
161 to the suppression of the large quantities of negatively charged functional oxygen groups
162 previously covering the GO during the thermal reaction with PEI-KOH. Indeed, the reduction
163 of GO, as suggested by the UV-Vis, FTIR and XPS analyses (discussed in the next section),
164 led to the partial reconstruction of the graphenic network; the sheets then tend to aggregate in
165 order to diminish the free energy (Huang et al., 2018). Additionally, hydrogen bonding
166 between the remaining oxygen and the amine groups of PEI might result in these crumpled
167 rGO sheets.

168 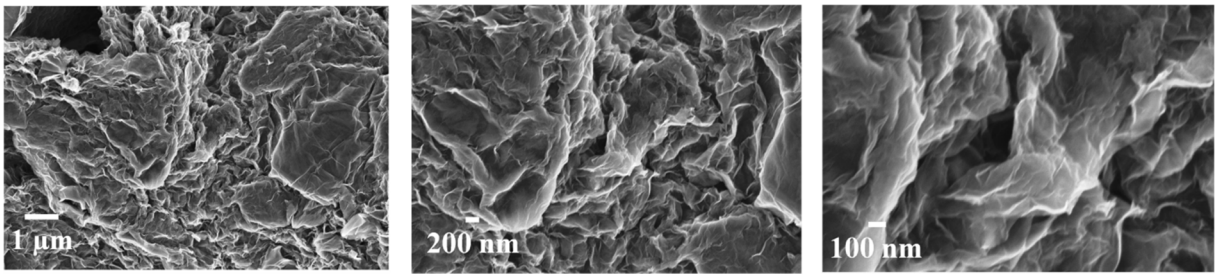

Figure 1. SEM images of rGO/PEI-KOH composite at low and high magnifications.

On the transmission electron microscopy (TEM) images of **Figure 2**, wrinkled graphene sheets (dark areas) are visible. The images also indicate that the graphene sheets were etched during the hydrothermal reduction-functionalization of GO; traces of nanopores can be seen in **Figure 2** (Lu et al., 2012; Sun et al., 2012). The nanopores formation is not fully clarified in this work as usually GO becomes porous during a process where strong radicals like hydroxyl radicals ($OH^{\bullet}$) are produced locally in the vicinity of rGO surface; these radicals are known to have ability to break the C–C (sp^2) bonds in the graphene sheet, causing its porosity and could even break GO into ultra-small graphene oxide of zero dimensions (Zhao et al., 2017). Many oxidation processes are able to produce these highly reactive hydroxyl radicals, such as photocatalysis, Fenton reactions, ozone, radiolysis, electron beam irradiation, sonolysis (Wu and Shi, 2010) and high voltage electrical discharge (Sahni and Locke, 2006). However, these strong radicals could also intervene during elaboration under hydrothermal conditions in basic media, as reported by Feng *et al.* (Feng et al., 2016).

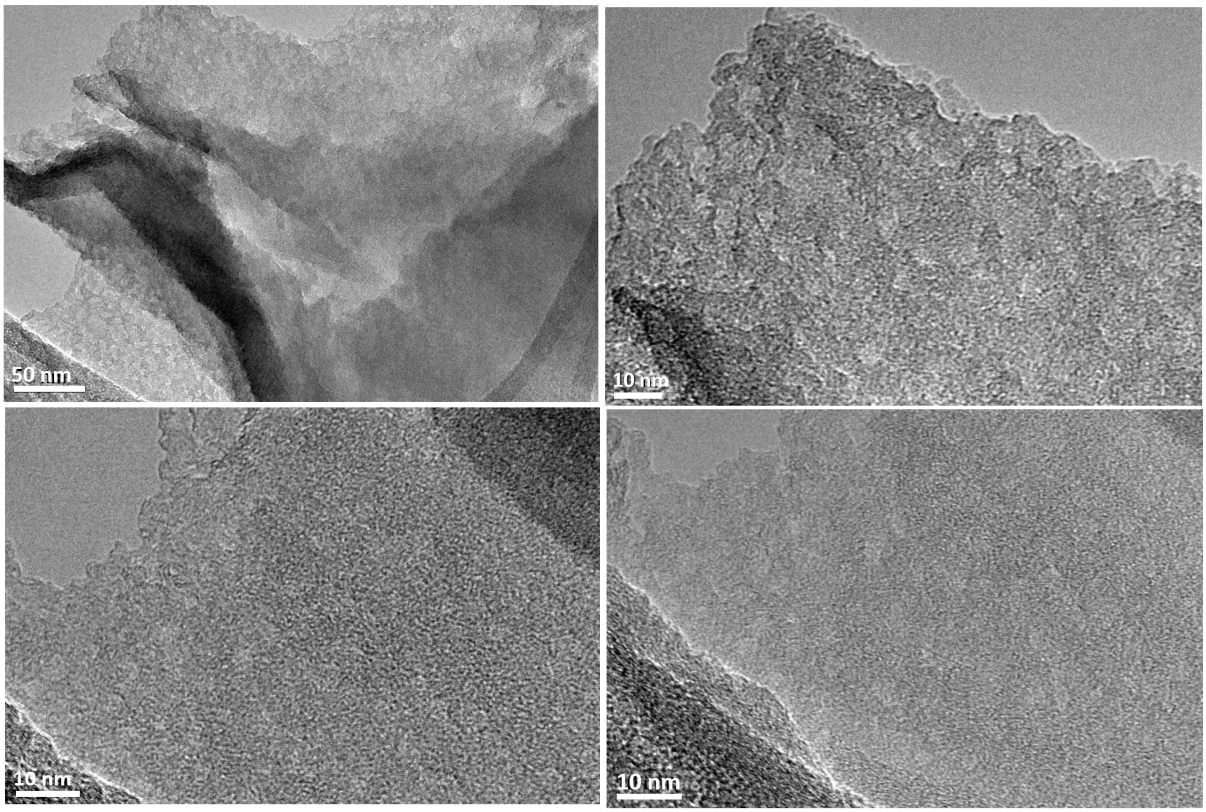

Figure 2. TEM images of rGO/PEI-KOH sheets at low and high magnifications.

The reduction of GO was monitored by UV-vis spectrophotometry. As shown in **Figure 3**, GO displays two bands at 235 nm due to the π–π* transition of aromatic C=C bonds, and 310 nm ascribed to the n–π* transition of C=O bonds (Fellahi et al., 2011). After PEI-KOH reduction-functionalization for 24 h, the peak related to the π–π* transition initially at 235 nm shifted to 258 nm; this red-shift in absorption peak takes place when the π electron conjugation is restored within the sheets of graphene. Furthermore, the shoulder in the spectrum disappears, signifying an important decrease of C=O bonds; these two features indicate the partial reduction of GO during the hydrothermal process.

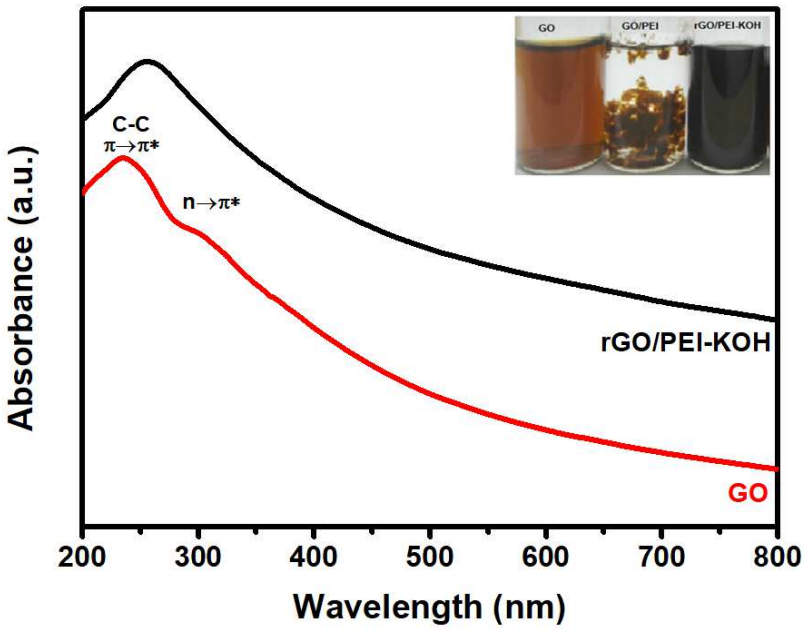

Figure 3. UV–vis spectra of GO and rGO/PEI-KOH in water. The inset exhibits the digital photographs of GO, GO-PEI and rGO/PEI-KOH dispersion in water.

Figure 4 shows the FTIR spectra of GO, PEI and rGO/PEI-KOH FTIR. The following functional groups were established in the FTIR spectrum of GO sample: O-H stretching vibrations in COOH group and/or intercalated water (3381cm^{-1}), C=O stretching vibration

(1736 cm^{-1}), aromatic stretching vibration of C=C bonds (1623 cm^{-1}), and C-O vibrations of epoxy and alkoxy groups at 1228 and 1056 cm^{-1}, respectively (Budimir et al., 2019).

After reduction-functionalization by PEI-KOH treatment, peak intensities associated with oxygen containing groups (O-H and C-O stretching vibrations) diminished significantly, which is a signature of effective GO reduction. In addition, the typical absorption features of the PEI at 2898 and 2970 cm^{-1} corresponding respectively to symmetric and asymmetric C-H stretching from the -CH_2 group of PEI were visible (Budimir et al., 2019). Moreover, the band at 1736 cm^{-1} nearly disappeared, and a new band attributed to the stretching vibration of N–H (in the C–NH group) appeared at 1575 cm^{-1} (Ramanathan et al., 2005; Budimir et al., 2019). Other observed peaks at around 1085 and 876 cm^{-1} are assigned to C–N bond stretching vibrations and CH_2 rock + N–H⊥ bending, respectively (York et al., 2003). These results clearly confirm that the GO was effectively reduced during the hydrothermal process and the PEI molecules were attached to the rGO sheets.

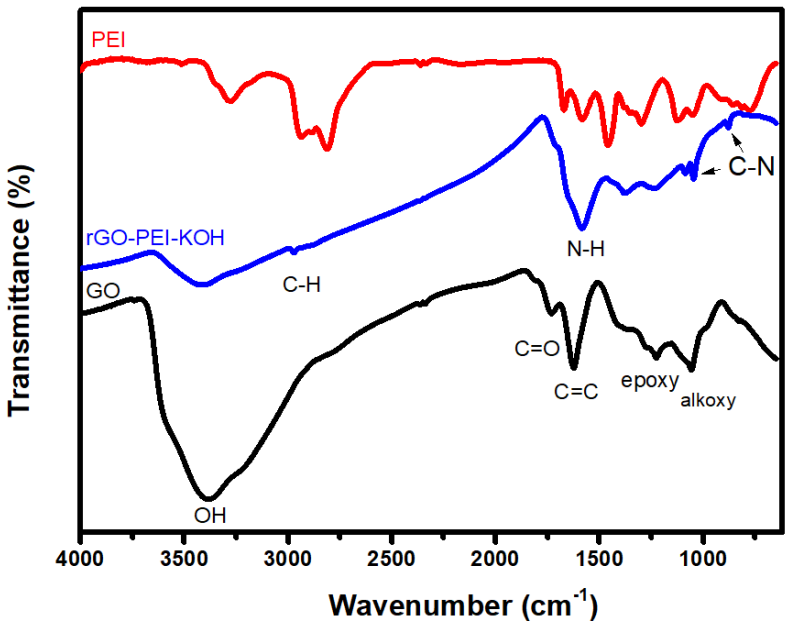

Figure 4. FTIR spectra of GO, PEI, and rGO/PEI-KOH.

The elemental composition of the as-elaborated PEI-KOH reduced-functionalized GO was examined using X-ray photoelectron spectroscopy (XPS). **Figure 5(a)** depicts the XPS spectra of GO and rGO/PEI-KOH. The spectrum of GO essentially comprises the C_{1s} and O_{1s} peaks at ~285 and ~532 eV, respectively. The peaks in the rGO/PEI-KOH XPS wide scan located at 285, 400 and 531 eV are ascribed to C_{1s}, N_{1s} and O_{1s}, respectively. The occurrence of tiny peaks attributable to K_{2p} and K_{1s} in the XPS spectrum originates most likely from potassium adsorption. Furthermore, the intensity of the oxygen peak was greatly reduced in the rGO/PEI-KOH as compared to GO, indicating an efficient reduction of GO by KOH-PEI treatment. The presence of a peak at 400 eV due to N_{1s} proves the successful grafting of PEI on the rGO sheets (Liu et al., 2013; Budimir et al., 2019). The atomic percentages of each element (C, O and N) in GO and rGO/PEI-KOH are summarized in **Table 1**.

The core level of the C_{1s} of GO can be deconvoluted into three distinct peaks centered at 284.8, 286.8 and 288.3 eV, which correspond to unoxidized graphite carbon skeleton (C–C), hydroxyl/epoxide groups (C–O) and carboxyl groups (C=O), respectively (**Figure 5b**) (Li et al., 2001; Liu et al., 2013). The reduction of GO is mainly indicated by three peaks in the C_{1s} core-level spectrum (**Figure 5c**) showing the same functional groups, but with decreased intensities of the groups containing oxygen: the sp^2-hybridized carbon atoms of graphene (C-Csp^2) at 284.6 eV, the carbon in hydroxyl and epoxide groups (C-O) at 286.5 eV, the carbonyl groups (C=O) at 287.8 eV, and the carboxyl (OH-C=O) groups at 288.9 eV (Liu et al., 2013). The band at 285.3 eV is assigned to C-N of the PEI molecules (Shao et al., 2016).

The N_{1s} high resolution peak showed a single component after fitting due to amine groups from PEI (**Figure 5d**).

Table 1. Elemental atomic percentage determined using the XPS spectra.

Composite	**C_{1s} at.%**	**O_{1s} at.%**	**N_{1s} at.%**

GO	69.93	30.07	-
rGO/PEI-KOH	80.13	16.68	3.19

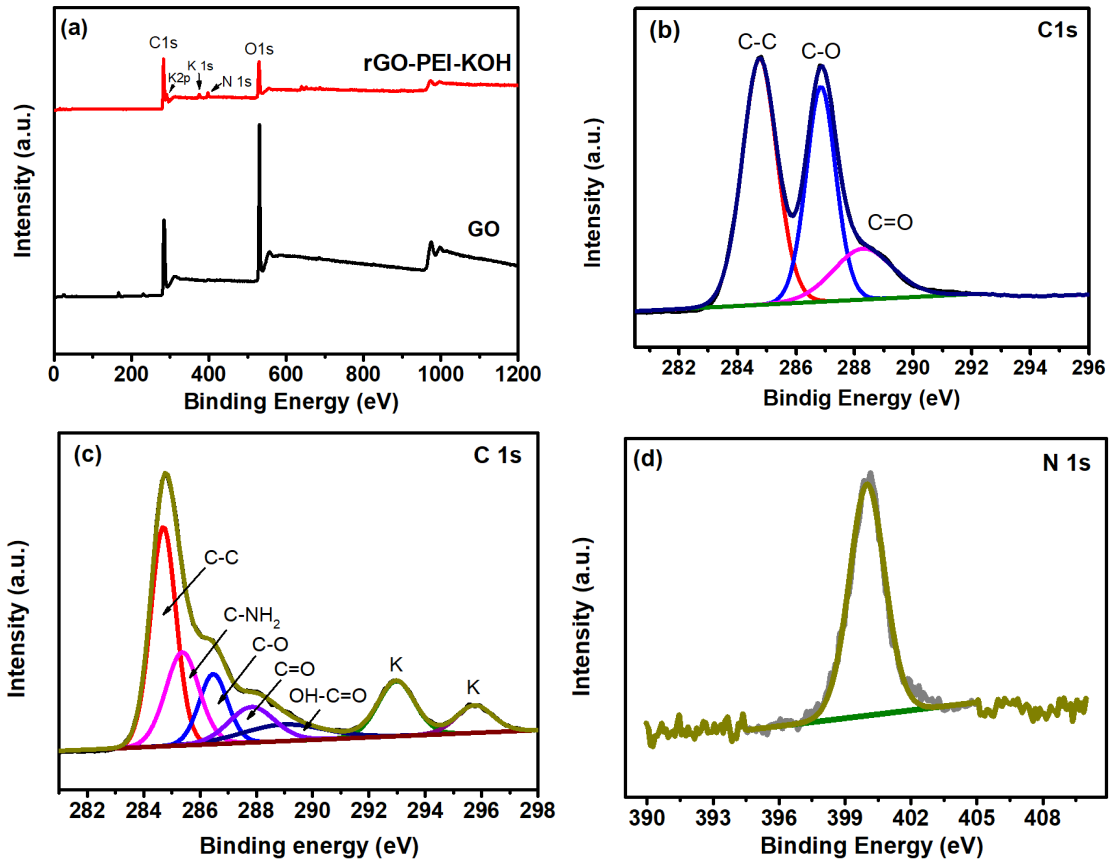

Figure 5. (a) XPS survey spectra of GO and rGO/PEI-KOH; core level spectra of (b) C_{1s} of GO, (c) C_{1s} and (d) N_{1s} of rGO/PEI-KOH.

The existence of a significant amount of K was identified by the presence of imposing peaks at 292.9 and 295.7 eV in **Figure 5c**. Since the binding energy discrepancy between these two peak components is ca. 2.8 eV, and their intensity ratio is ca. 2:1, they are attributed to the spin-orbit-split doublet $K_{2p1/2}$ and $K_{2p3/2}$, respectively of potassium cations and oxides (Li et al., 2001). This suggests that potassium ions probably bind to the remaining oxygen atoms or are intercalated within rGO sheets.

Raman spectroscopy is a powerful and widely employed technique for characterizing graphene based structures involving disorder and defects (Fang et al., 2013). The Raman spectra of GO and rGO/PEI-KOH are depicted in **Figure 6**. They indicate important structural changes in graphene sheets before and after treatment with PEI-KOH. It can be seen that the D peaks (disorder induced symmetry A_{1g} mode) of GO and rGO/PEI-KOH are located at 1360 and 1357.3 cm^{-1}, respectively, while the G bands (due to the E_{2g} mode associated with the bond stretching of sp^2-bonded carbon atoms in hexagonal, two-dimensional lattices) are at 1589.4 and 1590 cm^{-1}, respectively.

It is worth noting that the chemical changes in graphene-based materials are marked by variations in the D and G band ratios; these variations in the relative intensities of the D and G bands (D/G) reflect modifications in GO electronic conjugation state during the reduction-functionalization phase. Commonly, the ratio I_D/I_G serves to quantify the disorder level in graphene and rGO; this disorder can be related to vacations, impurities, dislocation, dangling bonds at the edges of the rGO sheets and to the decrease of the average size of the sp^2 domains, but can also be the signature of an augmentation of the C sp^3 hybridization caused by molecules grafted to the 2-D hexagonal carbon lattice. After the reduction-functionalization of GO with PEI-KOH, the intensity ratio I_D/I_G rises from 0.79 for GO to 1.13 for rGO/PEI-KOH. Usually, reducing GO consists mainly in the elimination of the oxygen functional groups (these later are known to induce sp^3 hybridization of the carbon atoms) from the graphene sheet; when the GO is reduced, sp^3 hybridization diminishes, and the graphene sheet is more or less restored, which is generally accompanied by a diminution in the I_D/I_G ratio. This is not the case in this work as a non-negligible augmentation of I_D/I_G is observed despite the fact that oxygen functionalities have been significantly eliminated as it was proven by XPS and FTIR analyses. We can speculate two reasons for this increase in I_D/I_G ratio: either it highlights the large presence of sp^3 carbon atoms on GO due the grafting

of PEI molecule, a signature of the mesoporosity and/or a decrease in the average size of the sp^2 domains in rGO sheets (Fang et al., 2013; Liu et al., 2013; Tong et al., 2015; Singh et al., 2017; Pakulski et al., 2018).

Also the red-shift of the D-band (from 1360 to 1357.3 cm^{-1}) testifies the actual functionalization of reduced GO (Budimir et al., 2019). Such results confirm that PEI was effectively grafted on the rGO layer during the reduction-functionalization process; these results are well consistent with the FTIR and XPS data.

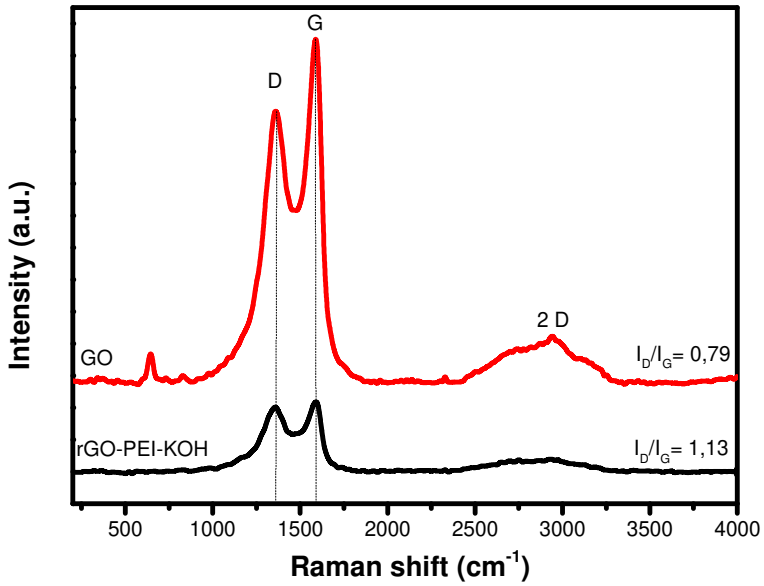

Figure 6. Raman spectra of GO and rGO/PEI-KOH.

The thermal behavior of the rGO/PEI-KOH was evaluated by thermogravimetric and differential thermogravimetric (TG/DTG) analysis. **Figure S1** exhibits the TG analysis curve of the as-prepared rGO-PEI-KOH, displaying different weight losses within the temperature range tested. The initial weight drop (15.4%) between ambient temperature and 150°C is more possibly caused by the evaporation of adsorbed water molecules. A second weight loss (7.4%), observed in the range 150-270°C, is related to the removal of oxygen-containing functional groups. Finally, the weight loss (12.8%) in the 270–550°C temperature range corresponds to the covalently bonded PEI molecules pyrolysis, suggesting that the rGO

surface was modified by PEI (Liu et al., 2013). The results confirm again the surface grafting of PEI molecules on rGO sheets.

3.2. Cr(VI) elimination performance of the rGO/PEI-KOH composite

3.2.1 Effect of adsorbent dosage

The effect of adsorbent dosage on the Cr(VI) removal, for a fixed pollutant concentration of 100 mg/L, was investigated and the results are displayed in **Figure 7**. The percentage of removal increases from 87.78 to 100% by increasing the adsorbent dosage from 0.5 to 2.5 mg/mL. For adsorbent dosage from 0.5 to 1 mg/mL, the removal efficiency increases until reaching ~100%; this means that the more adsorbent in the solution, the higher the availability of exchangeable sites for metal ions (Sandhya and Tonni, 2004).

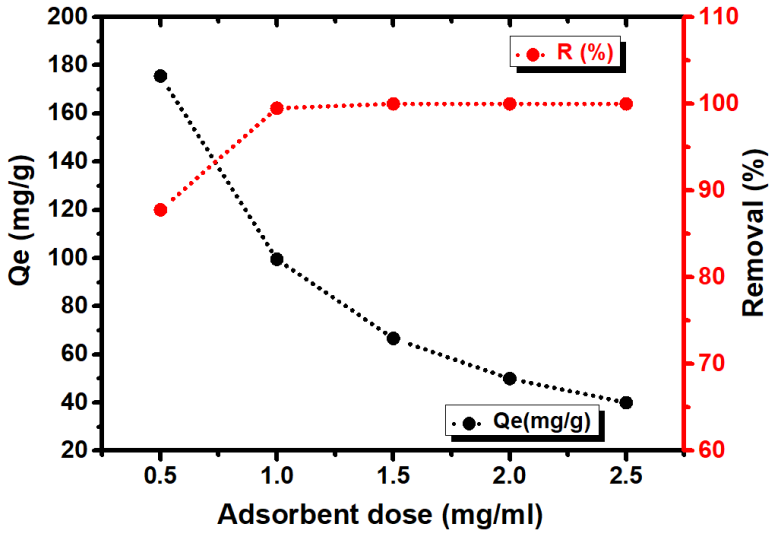

Figure 7. Effect of rGO/PEI-KOH dosage on the capacity of adsorption (Q_e) and removal efficiency (R) (initial Cr(VI) concentration: 100 mg/L, pH 2, room temperature, contact time: 24 h).

On the other hand, the adsorption capacity Qe shows a clear decrease, suggesting a possible formation of microscopic agglomerates of rGO/PEI-KOH sheets that would reduce the access to all adsorption sites. Exceeding the adsorbent dosage of 1 mg/mL, the removal efficiency

remains roughly at ~100%, while the adsorption capacity continues dropping; this is expected given the presence of more adsorbent than what is necessary to remove all the pollutant.

3.2.2 pH effect

The adsorption tests were carried out at an initial concentration of Cr(VI) of 100 mg/L, a 24 h contact time, an adsorbent dosage of 1 mg/mL, in the pH range from 2 to 9 at room temperature. The solution pH greatly affects the stability of Cr(VI) species and the adsorbent charge, thereby affecting the adsorption efficiency. **Figure 8a** illustrates the predominance diagram of $K_2Cr_2O_7$ in water at different pH values. It indicates that the prevailing forms of Cr(VI) ion in solution are chromate $(CrO_4)^{2-}$, dichromate $(Cr_2O_7)^{2-}$, and hydrogen chromate $(HCrO_4)^-$ and predominant ions are related to the solution pH and overall concentration of chromate. Cr(VI) is in the form of anionic species, like $HCrO_4^-$ (pH range 2.0–7.0) and CrO_4^{2-} (pH range 7.0–10.0) (Fan et al., 2012) are the dominant species.

Figure 8b displays the zeta potential of rGO/PEI-KOH at different pH values. The rGO/PEI-KOH sheets are globally negatively charged even they are grafted with PEI molecules, which are positively charged at low pH. Indeed, the amine groups are protonated under strong acidic conditions, which is beneficial for the Cr(VI) anions adsorption through electrostatic interactions. In contrast, uncharged ($–NH_2$) or deprotonated ($–NH^-$) groups, occurring under basic conditions, will repel these anions thus inhibiting their adsorption. On the other hand, the overall negative charge of the adsorbent sheets remains beneficial, and even necessary, as it will supply the adsorbent with H^+ ions necessary for the Cr(VI) reduction, as we will be seen in the last section (Luo et al., 2017; Wang et al., 2017).

Figure 8c depicts the adsorption capacity at different pH values. We can notice the absence of Cr(VI) removal by rGO/PEI-KOH for a pH value higher or equal to 3. Indeed, upon increasing the pH from 3 to 9, the divalent CrO_4^{2-} amount rises by gradual conversion of

348 $HCrO_4^-$; also the protonation degree of the surface is weakened under weak-acidic/basic
349 conditions, resulting in greater electrostatic repulsion between ions charged negatively and the
350 adsorbent surface (Zhou et al., 2016). Nevertheless, strong acid conditions corresponding to
351 pH lower or equal to 2 is beneficial for Cr(VI) elimination by rGO/PEI-KOH as it promotes
352 more positive amine groups and less negative Cr(VI) species.
353 Hence, the pH of the solution, which greatly influences the stability of Cr(VI) species and the
354 electrostatic charge of the adsorbent, impacts significantly the adsorption efficiency. The pH
355 2, being the optimal one, was used for all subsequent experiments.

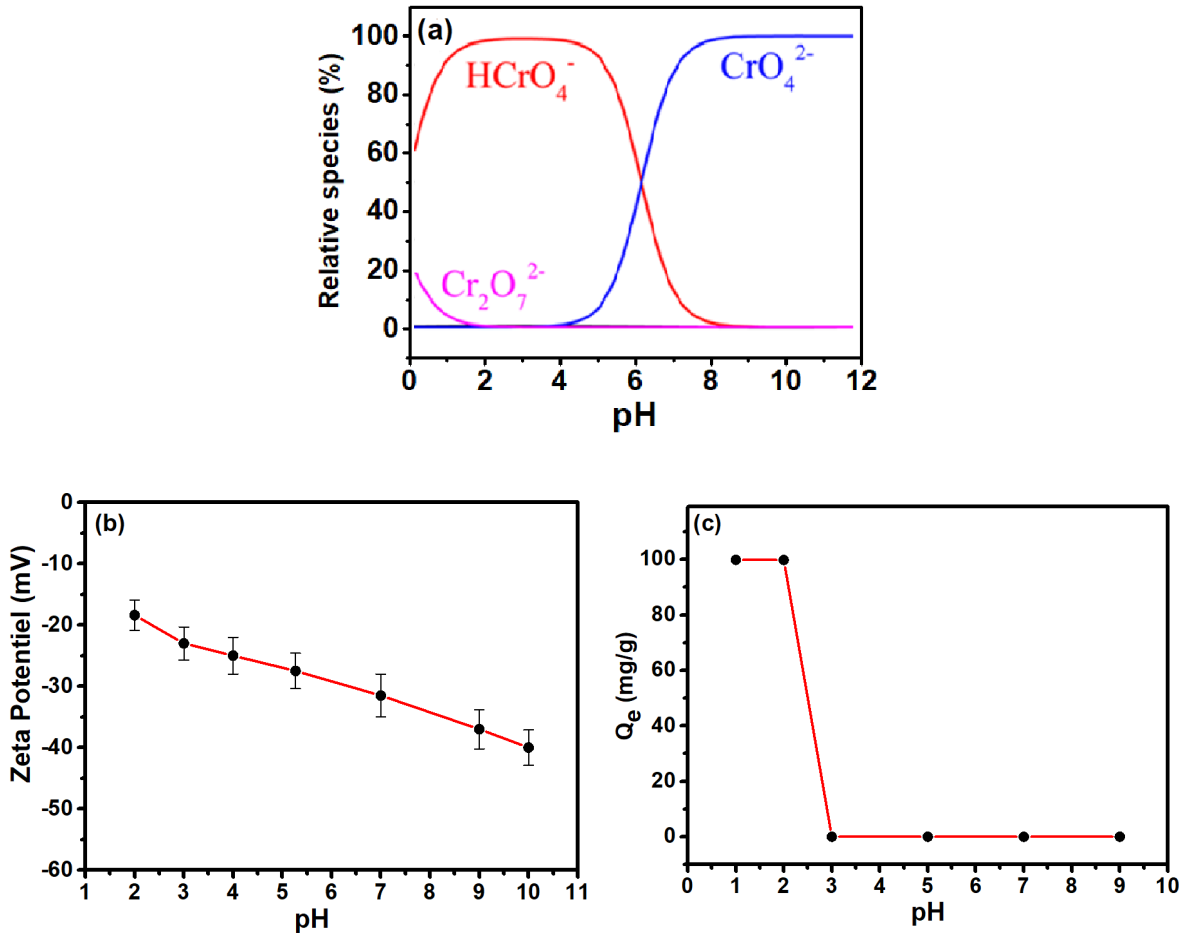

356
357
358 **Figure 8.** (**a**) Cr(VI) species predominance diagram as a function of pH; (**b**) Zeta potential of
359 rGO/PEI-KOH; (**c**) Adsorption capacity at different pH (initial Cr(VI) concentration:
360 100 mg/L, adsorbent dosage: 1 mg/mL, room temperature, contact time: 24 h).
361

3.2.3 Initial concentration effect

The influence of the initial Cr(VI) concentration on adsorption capacity of rGO/PEI-KOH is depicted in **Figure 9**; the Cr(VI) ions are adsorbed favorably on the rGO/PEI-KOH surface at pH 2. The adsorption capacity of rGO/PEI-KOH increases rapidly with increasing the initial concentration of Cr(VI) from 100 to 700 mg/L, implying that there are enough adsorption sites on the adsorbent and attesting the attraction effectiveness between the protonated adsorbent and the hydrochromate anion. The results revealed that the Cr(VI) maximum adsorption capacity of rGO/PEI-KOH is (398.9±16.9 mg/g) at room temperature, which is greater than the capacity of PEI-modified graphene (324 mg/g), as shown in the last section.

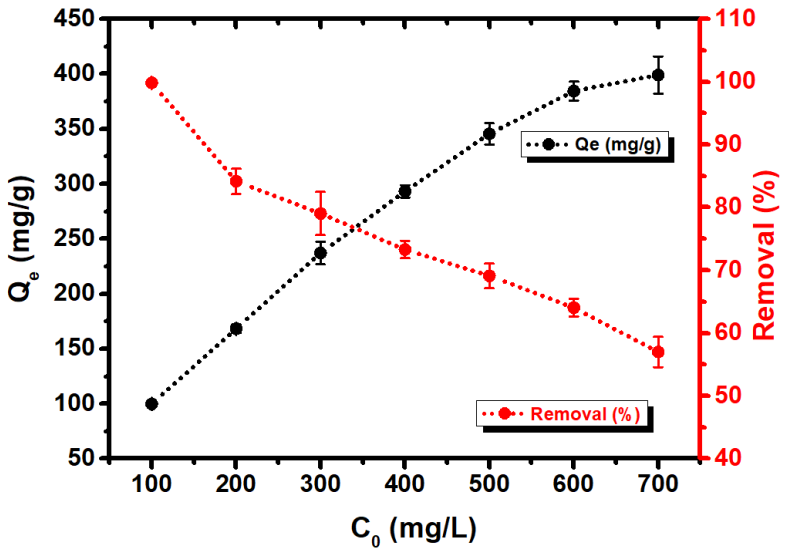

Figure 9. Effect of initial Cr(VI) concentration on the adsorption capacity (black) and the removal efficiency (red) of rGO/PEI-KOH (pH 2, adsorbent dosage: 1 mg/mL, room temperature, contact time: 24 h).

On the other hand, the removal efficiency decreases with the increase of Cr(VI) concentration. This is most likely related to the total available adsorption sites, since they are limited for a fixed adsorbent dose and consequently we approach saturation at a higher Cr(VI) concentration.

3.2.4 Adsorption isotherm study

The adsorption equilibrium data give very important information needed to understand the adsorption process correctly. The understanding of adsorption isotherms is important for optimizing the adsorption process pathways and implementing adsorption systems effectively (Ayawei et al., 2017). Hence, the linear and nonlinear forms of modified-Langmuir, Temkin, Freundlich and Dubinin-Radushkevich isotherm models were used to fit experimental data; C_e (mg/L) and Q_e (mg/g) are the equilibrium Cr(VI) concentration and adsorption capacity, respectively; the initial concentration of Cr(VI) is represented by C_0 (mg/L).

The classic Langmuir adsorption isotherm was derived for the gas phase adsorption process. It supposes a homogeneous surface where the binding sites have the same energy and affinity (equivalency of the adsorption sites) and where adsorption occurs in a monolayer; also it assumes that adsorbed molecules do not interact with each other (Langmuir, 1918; Luo et al., 2017). Recently, a modified Langmuir equation has proved to me more applicable for modeling liquid adsorption data. This model is given according to the following equations (Azizian et al., 2018):

$$\frac{C_e}{Q_e} = \frac{(K_{ML}-1)C_e}{K_{ML}Q_m} + \frac{C_s}{K_{ML}Q_m} \quad (3)$$

$$Q_e = \frac{Q_m K_{ML} C_e}{(C_s-C_e) + K_{ML}C_e} \quad (4)$$

Where Q_m is the maximum adsorption capacity, C_s is the saturation concentration of Cr(VI) in liquid-phase (45,000 mg/L) and K_{ML} is the constant of modified Langmuir.

By linear and nonlinear fittings, the Q_m capacity and K_{ML} constant are extracted from experimental data (**Figure 10a** and **10e**) and presented in **Table 2**; Q_m obtained is close to the experimental value (398.9 ±16.9 mg/g).

The modified-Langmuir isotherm parameters as well as the regression coefficient obtained (**Table 2**) suggest Adsorptive Interaction Effectiveness between the protonated rGO/PEI-KOH adsorbent and the hydrochromate anion.

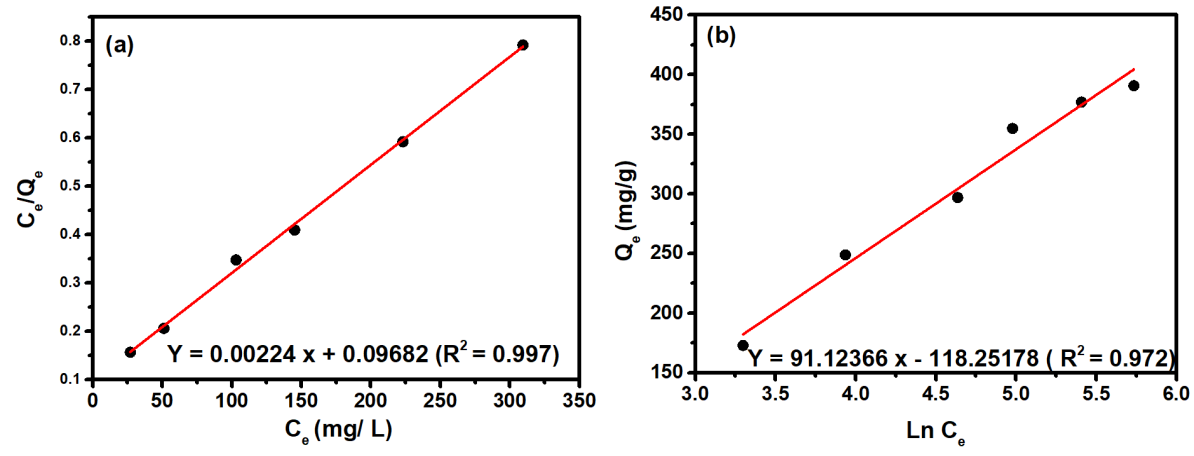

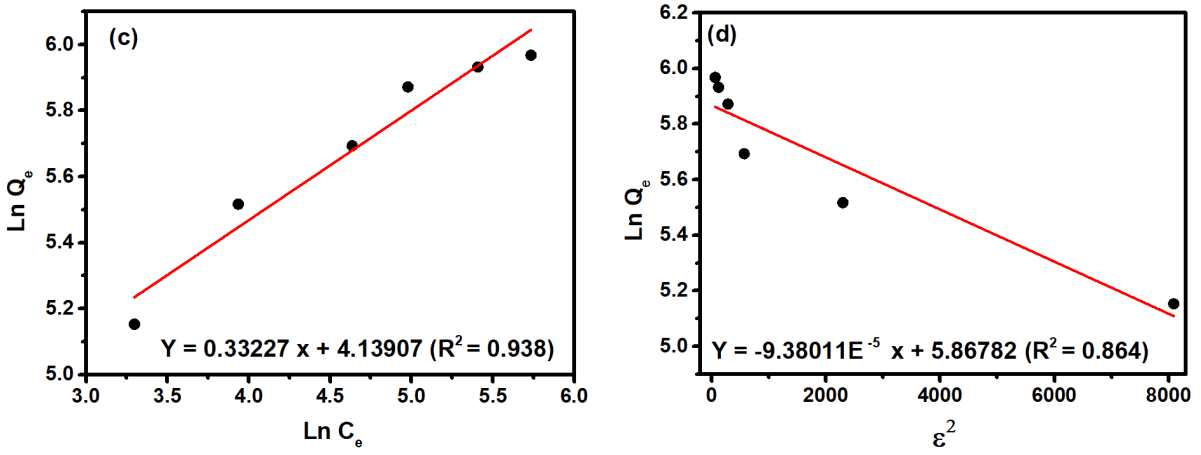

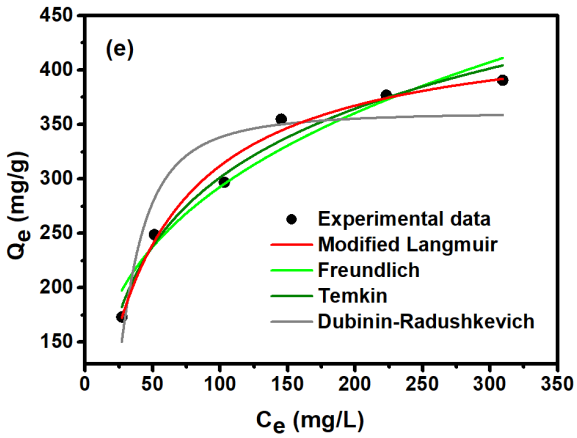

Figure 10. Linear fitting of (a) modified-Langmuir, (b) Temkin, (c) Freundlich, (d) Dubinin-Radushkevich and (e) nonlinear fitting of adsorption isotherm models (pH 2, adsorbent dosage: 1 mg/mL, room temperature, contact time: 24 h).

The Temkin model of isotherm takes into-account the effects of the interaction between adsorbed molecules in the adsorption process. The adsorption energy (ΔH_{ads}) in this model displays a linear decrease when surface coverage rises, due to adsorbent–adsorbate interactions (Ayawei et al., 2017; Darabi et al., 2018). The following equations give the nonlinear and linear forms of the Temkin isotherm model (Temkin, 1941):

$$Q_e = ALn(K_T C_e) \quad (5)$$

$$Q_e = A\, lnK_T + A\, lnC_e \quad (6)$$

$$A = \frac{RT}{b} \quad (7)$$

Where A is related to the Temkin constant b corresponding to the adsorption heat, K_T is the Temkin isotherm equilibrium binding constant, R is the gas constant and T is the temperature (Darabi et al., 2018). K_T and A are extracted from the linear and nonlinear fittings (**Figure 10b and 10e**), whose values are reported in **Table 2**. The positive sign of b indicates an exothermic process (Ferrandon et al., 1995), and its value (27.19 kJ/mol) suggests that chemisorption may be an important part of the adsorption process (Ho et al., 2002).

The isotherm of Freundlich (Freundlich, 1906) is used when adsorption occurs on surfaces that are heterogeneous, showing a non-uniform adsorption heat distribution. The expression describing this isotherm encompasses the heterogeneity of the surface and the active sites (and their energy) exponential distribution. The Freundlich sorption isotherm is given by the equations (8, 9) (Ayawei et al., 2017; Darabi et al., 2018):

$$Q_e = K_F C_e^{1/n} \quad (8)$$

$$lnQ_e = \frac{1}{n}\, lnC_e + lnK_F \quad (9)$$

435 Where the constant K_F is related to the relative adsorption capacity of the adsorbent and n is a
436 constant indicating the adsorption intensity (the lower the 1/n value the stronger the
437 adsorption intensity (Darabi et al., 2018)). The linear and nonlinear fittings allow obtaining
438 easily these constants (**Figure 10c** and **10e**) whose values are summarized in **Table 2**. The
439 isotherm of Freundlich is extensively used in heterogeneous systems, the value of (1/n)
440 ranging from 0 to 1 may be an indicator of the degree of surface heterogeneity, surface being
441 more heterogeneous as (1/n) approaches zero (Foo and Hameed, 2010). The 1/n value
442 obtained here (0.33) is closer to zero than to unity and may imply a chemisorption process
443 (Foo and Hameed, 2010).
444 The Dubinin–Radushkevich (D-H) isotherm is usually used to describe the mechanism of
445 adsorption onto a heterogeneous surface with a Gaussian energy distribution. Generally, this
446 isotherm is expressed as follows (Ho et al., 2002; Foo and Hameed, 2010):

447 $$Q_e = Q_D \exp(-B_D \varepsilon^2) \quad (10)$$

448 $$lnQe = lnQ_D - B_D \varepsilon^2 \quad (11)$$

449 where Q_D is the maximum adsorption capacity, the activity coefficient B_D is related to mean
450 sorption energy, ε^2 is Polanyi potential. By fitting (**Figure 10d** and **10e**), B_D is extracted from
451 the slope of the fitting and Q_D from the intercept.
452 The ε is estimated using Eq.12:

453 $$\varepsilon = RTln\left[1 + \frac{1}{C_e}\right] \quad (12)$$

454 where R, T and C_e represent the gas constant, absolute temperature and adsorbate equilibrium
455 concentration, respectively.
456 The mean sorption energy E necessary to detach a molecule from its position in the sorption
457 space to the infinity, which is a measure of the nature of adsorption (physical or chemical) is
458 expressed as:

459 $$E = \frac{1}{\sqrt{2B_D}} \quad (13)$$

460 The E value, determined using equation (13), is 73 kJ/mol. The Q_D value (353.47 mg/g) is
461 consistent with both the Q_{max} value (446 mg/g) previously determined with the modified-
462 Langmuir isotherm and the experimental one (398.9±16.9 mg/g).
463 The results provided in **Table 2** show that the regression coefficient R^2 in the Dubinin-
464 Radushkevich (0.864) is lower than that of modified-Langmuir, Temkin and Freundlich
465 fittings, indicating that D-H data do not correlate as well as for the previous isotherms. The
466 Cr(VI) removal simulation data using the modified-Langmuir model (R^2 = 0.997) are better
467 than those obtained by the Freundlich (R^2 = 0.938) and the Temkin (R^2 = 0.972) models,
468 demonstrating that Cr(VI) adsorption process on rGO/PEI-KOH is best fitted by the modified-
469 Langmuir model; this result indicates that Cr(VI) sorption onto rGO/PEI-KOH is not
470 exceeding a monolayer coverage on a homogeneous surface with active sites well distributed
471 throughout.

472 **Table 2.** Isotherm rate constants and regression coefficients for different models.

Models	Parameters	Linear	Nonlinear
Langmuir	Q_{max} (mg/g)	446.00	445.97
	K_{ML} (L/mg)	1042.10	1047.11
	R^2	0.997	0.982
Temkin	A (unitless)	91.12366	91.11
	K_T (L/mg)	0.27	0.27
	b (kJ/mol)	27.1891	27.1
	R^2	0.972	0.972
Freundlich	K_F (mg/g) $(L/mg)^{1/n}$	62.74	73.30
	n	3	3.32
	R^2	0.938	0.933
Dubinin-	Q_m (mg/g)	353.47	361.96
Radushkevich	B (mol^2/kJ^2)	$9.38011E^{-5}$	$6.6496E^{-5}$

	E (kJ/mol)	73	86.71
	R^2	0.864	0.829

3.2.5 Effects of contact time and adsorption kinetics study

Cr(VI) kinetics of adsorption on rGO/PEI-KOH are estimated with the pseudo-first and second order models by fitting kinetic experimental data. Thereby, the influence of the contact time on Cr(VI) adsorption was studied (Cr(VI) concentration: 100 mg/L at pH 2.0). **Figure 11a** reveals that the capacity of adsorption rises rapidly within the first 4 h; afterward, it continues to raise slowly and approaches equilibrium at around 24 h. Both the kinetic models, pseudo-first-order and second-order, are given by the following equations (Ho and Mckay, 1999; Azizian, 2004):

Pseudo-first-order:

$$Q_t = Q_e(1 - e^{-K_1 t}) \quad (14)$$

Pseudo-second-order:

$$Q_t = \frac{Q_e^2 K_2 t}{1 + Q_e K_2 t} \quad (15)$$

Where Q_e is the quantity of adsorbed pollutant at equilibrium, Q_t is the amount of adsorption at t time, and K_1 and K_2 are the pseudo-first order and pseudo-second order rate constant, respectively.

The nonlinear fitting of the kinetic data is presented in **Figure 11a** and the obtained kinetic parameters are listed in **Table 3**. The comparison of the regression coefficient (R^2) values revealed that the adsorption kinetics of Cr(VI) onto rGO/PEI-KOH are well-described with the pseudo-second-order model. In addition, the absorption capacity ($Q_{e.cal}$=94.67 mg/g), calculated from the pseudo-second order kinetic model, is closer to that obtained experimentally ($Q_{e.exp}$= 99.38 mg/g). This result is predictable, because this model is adequate for a concentration of solute not too high as it is the case in this work (Azizian, 2004).

In order to investigate the mechanism of mass transfer during the adsorption process, the Weber-Morris model for intraparticle diffusion (Ho and Mckay, 1999; El Ouardi et al., 2019) was used. Weber-Morris stated that if intra-particle diffusion is the rate-controlling factor during an adsorption process, uptake of the adsorbate varies with the square root of time (equation (16)).

$$Q_t = K_{int} t^{1/2} + C \qquad (16)$$

Where K_{int} is the intraparticle diffusion rate constant. **Figure 11b** shows that the plots of Q_t *versus* $t^{1/2}$ are multi-linear, indicating that Cr(VI) adsorption mechanism occurs in three distinct stages. The first stage with the largest slope (K_{int1}) is due to an important diffusion of Cr(VI) anions from the solution to the intraparticle regions; the R^2 value indicates that at this first step of the adsorption process, the intraparticular diffusion is the predominant factor. The second linear stage, with lower K_{int} and R^2 values, suggest that the intraparticle diffusion becomes less predominant, this is probably linked both to the decrease in the Cr (VI) concentration gradient between the intraparticle regions and the solution, as well as a diminution of the available adsorption sites (intraparticle). For the final stage, with the lowest K_{int} and R^2, the process evolution ultimately resulted in a non-predominant intraparticle diffusion as the system approaches equilibrium. This is presumably due to a drop in the concentration gradient (between solution and intraparticle regions) as well as the almost-saturation of the intraparticle adsorption sites.

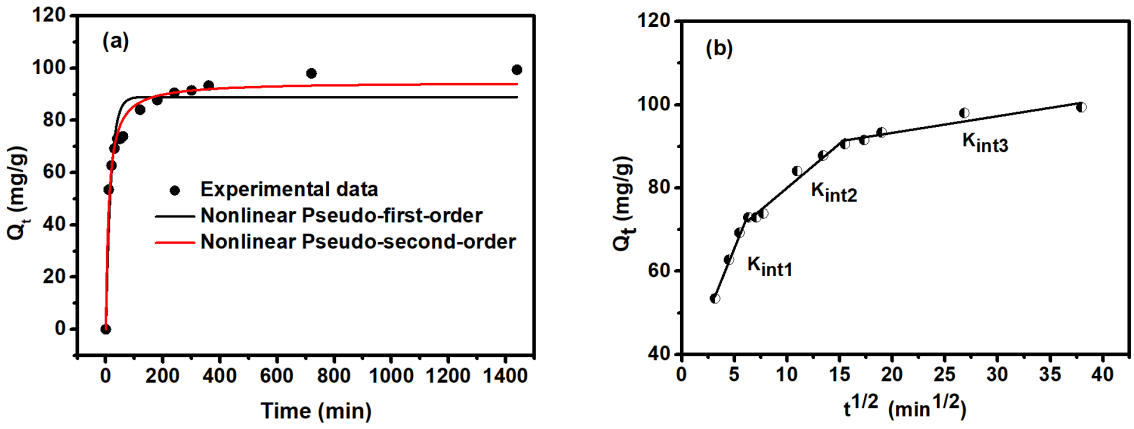

Figure 11. (a) Pseudo-first-order and pseudo-second-order nonlinear fitting and (b) intraparticle diffusion linear fitting for Cr (VI) adsorption onto rGO/PEI-KOH (pH: 2, concentration of Cr(VI): 100 mg/L, adsorbent dosage 1 mg/mL, room temperature, time of contact 24 h).

Table 3. Cr(VI) kinetic adsorption parameters onto rGO/PEI-KOH.

Kinetic models	**Parameters**	
Pseudo-first-Order		
	K_1 (min^{-1})	0.056
	Qe.cal(mg/g)	88.96
	R^2	0.898
Pseudo-second-Order		
	K_2 (g/mg min)	0.0009
	Qe.cal (mg/g)	94.67
	R^2	0.975
Intraparticle diffusion		
	K_{int1} (mg/g $min^{1/2}$)	6.24
	C_1	34.25
	R^2	0.991
	K_{int2} (mg/g $min^{1/2}$)	2.13
	C_2	58.70
	R^2	0.973
	K_{int3} (mg/g $min^{1/2}$)	0.40
	C_3	85.19
	R^2	0.892

3.2.6 Cr(VI) adsorption-reduction mechanism

To further analyze the Cr(VI) elimination mechanism by rGO/PEI-KOH, XPS was used to examine the elemental composition after the adsorption of Cr(VI). As shown in **Figure 12a**, the peaks of Cr_{2p} appear in the solid material, confirming that Cr(VI) is adsorbed successfully onto the material. The XPS spectrum of the Cr_{2p} further indicates that there are four components at 577.4, 580.2, 586.9 and 590.6 eV. The peaks at 577.4 and 580.2 eV represent $Cr_{2p3/2}$ orbitals, while the components at 586.9 and 590.6 eV are due to $Cr_{2p1/2}$ orbitals. The 577.4 and 586.9 eV peaks are ascribed to Cr(III), while 580.2 and 590.6 eV peaks are related to Cr(VI) (Ma et al., 2012; Zhang et al., 2013; Nezar et al., 2019). These results clearly indicate that both Cr(VI) and Cr(III) ions coexist on the rGO/PEI-KOH surface with 70.3 at% of Cr(III) of the total amount of adsorbed chromium, signifying a good reduction of the adsorbed pollutant.

Figure 12b displays the high-resolution N_{1s} XPS spectrum of rGO/PEI-KOH composite prior to and after Cr(VI) elimination. Before adsorption, the spectrum consists of one peak corresponding to N_{1s} of the amine group. After adsorption process in acidic conditions (pH 2), the N_{1s} can be deconvoluted into two peaks: a preponderant peak related to the amine group slightly shifted to higher binding energy, and a second peak at 401.4 eV due to the protonated amine groups ($-NH_3^+$). As explained above, at this pH value and $K_2Cr_4O_7$ concentration used, the chromium predominant species is the hydrochromate anion, $HCrO_4^-$, and it is worth noting that at this acidic pH, the PEI molecule is known to present a maximum protonation of amine groups, almost all these groups become positively charged (Curtis et al., 2016).

The $HCrO_4^-$ anions are electrostatically attracted to the protonated amine groups where they will be adsorbed, as illustrated by equation (17) (Wang et al., 2017):

$$-NH_3^+ + HCrO_4^- \longrightarrow NH_3^+ \cdots HCrO_4^- \qquad (17)$$

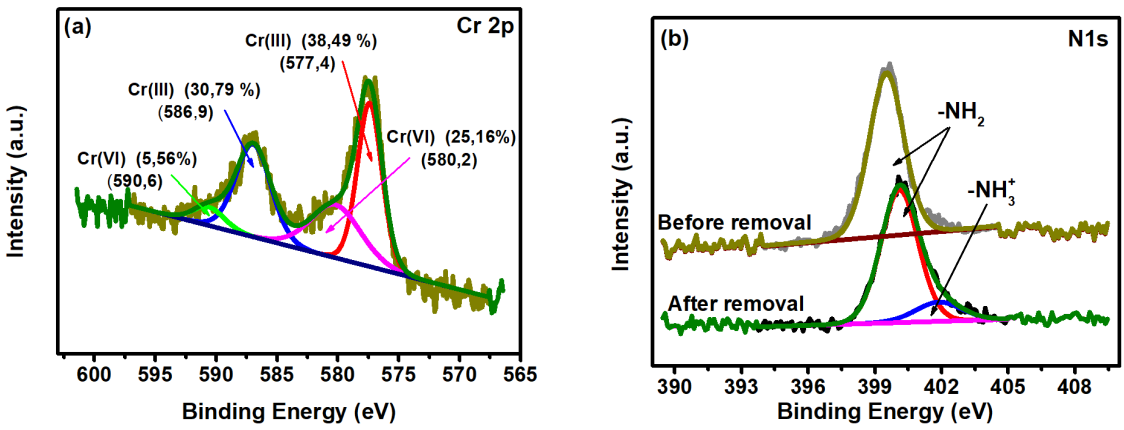

Figure 12. Core level XPS spectra of (a) Cr_{2p} and (b) N_{1s} of the rGO/PEI-KOH adsorbent before and after adsorption of Cr(VI).

Afterwards, Cr(VI) reduction takes place resulting in Cr(III) formation thanks to π-electrons of rGO, which serves as a donor of electrons in the Cr(VI)/Cr(III) reduction process (Ho et al., 2002; Ma et al., 2012; Darabi et al., 2018), according to equation (18):

$$HCrO_4^- + 7H^+ + 3e^- \longrightarrow Cr^{3+} + 4\,H_2O \qquad E^0 = +1.35\ V \qquad (18)$$

This E^0 positive value indicates that Cr(VI) is a strong oxidant at this low pH. Also, it can be noticed from equation (18) that the reduction of Cr(VI) is concomitant with an important consumption of protons; we presume that this property may explain that most amine groups are deprotonated after adsorption (**Figure 11b)**, but it does not explain why they are not reprotonated as it is expected in this still relatively acidic medium (Curtis et al., 2016). A possible response is given by the equation (19) (Deng and Ting, 2005; Zhao et al., 2016):

$$-NH_2 + Cr^{3+} \rightarrow -NH_2Cr^{3+} \qquad (19)$$

This equation illustrates the chelation between Cr(III) species and the deprotonated amine groups ($-NH_2$), thus preventing an ulterior reprotonation; a chelated complex may be formed by coordination between newly formed Cr(III) and $–NH_2$ group thanks to the fact that Cr(III) cation has an empty orbital and the amine group has a lone pair of electrons (Dai et al., 2012).

On the other hand, we speculate that the blue shift observed for the N_{1s} of the amine group after chromium adsorption is related to this chelation.

Scheme 2 illustrates the adsorption/reduction process, and **Table 4** depicts the values of some other adsorbent capacities for Cr(VI) reported in the literature. We can clearly see that the adsorption capacity of 398.9±16.9 mg/g at ambient temperature is among the highest recorded values.

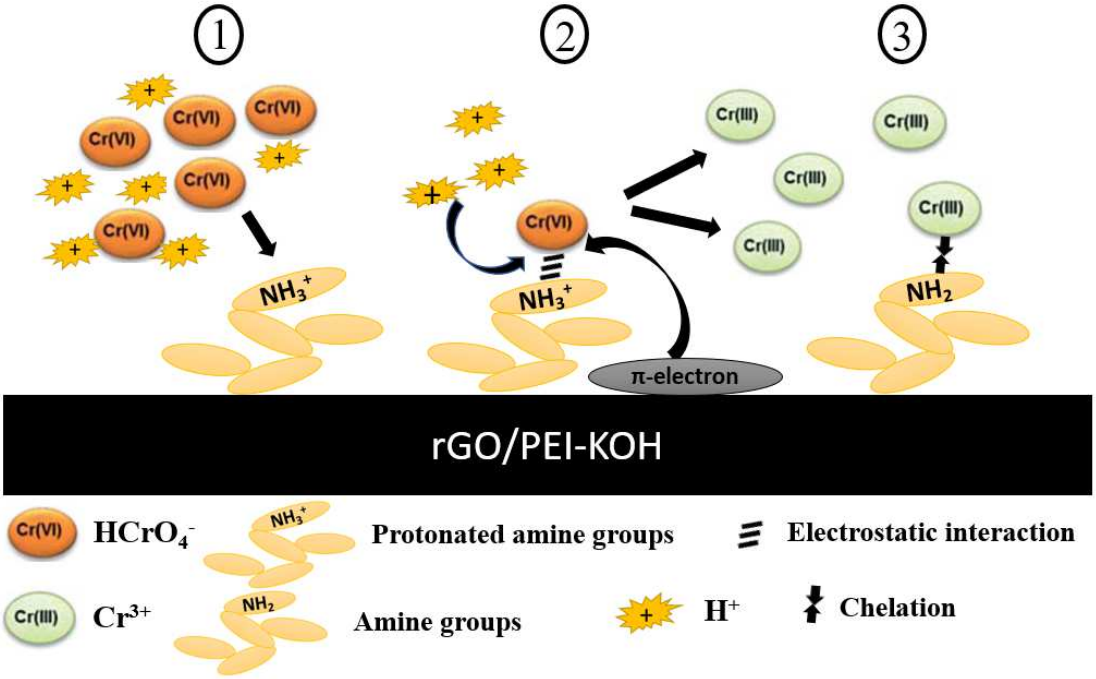

Scheme 2. Schematic illustration of the mechanism of Cr(VI) removal by rGO/PEI-KOH.

583

584

585

586

587

588 **Table 4.** The maximum adsorption capacity of Cr(VI) compared with some indicative

589 reported works.

Adsorbent	**Q_{max} (mg/g)**	**Reference**
Mesoporous carbon microspheres	156.3	(Zhou et al., 2016)
RGO/PEI/Fe_3O_4	266.6	(Wang et al., 2017)
Commercial activated carbon (CAC)	15.47	(Sandhya and Tonni, 2004)
KOH-modified carbonized Eucalyptus sawdust	45.88	(Zhang et al., 2018a)
PEI-modified-biomass of *Penicillium chrysogenum*	279.2	(Deng and Ting, 2005)
Iron nanoparticle decorated graphene	162	(Jabeen et al., 2011)
P(TA-TEPA)-PAM-RGO	397.5(35°C)	(Zhang et al., 2018b)
3-aminopropyltriethoxysilane-functionalized graphene oxide (AS-GO)	215.2	(He et al., 2017)
Magnetic β-cyclodextrin/graphene oxide nanocomposite (MCGN)	120.1	(Fan et al., 2012)
ED/DMF/rGO	92.15	(Zhang et al., 2013)
Amino functionalized graphene oxide decorated with Fe_3O_4 nanoparticles (AMGO)	123.4	(Zhao et al., 2016)
Reduced graphene oxide–montmorillonite (GCM)	12.86	(Zhang et al., 2015)
Polyethyleneimine modified eggshell membrane (PEI–ESM)	160	(Liu and Huang, 2011)
Ionic liquid modified reduced graphene oxide (IL-rGO)	232.55	(Nasrollahpour et al., 2017)
Sulfonated magnetic graphene oxide (SMGO)	222.22	(Alizadeh et al., 2017)
Graphene/MgAl-layered double hydroxides	172.55	(Yuan et al., 2013)

(G–MgAl-LDH)		
Triethylenetetramine modified graphene oxide/ chitosan composite (TGOCS)	219.5	(Ge and Ma, 2015)
rGO-PEI-KOH	**398.9 (25°C)**	**This work**
rGO-PEI	**324.0 (25°C)**	**This work**

590

591

592 ## 4. Conclusion

593 A graphene-based adsorbent was elaborated by reacting graphene oxide (GO) with
594 polyetheylenimine (PEI) and potassium hydroxide (KOH) at 90°C. Under these experimental
595 conditions, GO sheets were partially reduced while being at the same time functionalized with
596 PEI moieties. XPS, Raman, FTIR and TGA characterization proved an appreciable
597 deoxygenation of GO as well as the effective grafting of PEI on the rGO sheets. The as-
598 prepared rGO/PEI-KOH adsorbent exhibits an adsorption capacity of 398.9 mg/g for Cr(VI)
599 at room temperature. Compared to other works in the literature, this value is among the
600 highest reported. This adsorption is mainly attributable to the electrostatic interactions
601 between the chromium anion species and the low pH induced protonation of amine groups.
602 The isotherm plots suggest that during Cr(VI) sorption process rGO/PEI-KOH shows a
603 homogeneous surface where active sites are well distributed throughout; also, the results
604 suggest that chemisorption may play a non-negligible role in this process. Investigating the
605 adsorption kinetics, we found that it follows pseudo-second order model, which is consistent
606 with the Cr(VI) concentration range used. In addition, by applying the Weber-Morris model,
607 we noticed that intraparticle diffusion phenomena play a predominant role in the initial phase
608 of Cr (VI) adsorption. The subsequent Cr(VI) reduction to Cr(III), which attained 70.3% of
609 the total adsorbed chromium, is related to the oxidative action of the hydrochromate anion on
610 the rGO/PEI-KOH sheet, since this later acts as electron donor (π electrons). The results of

this work represent an interesting way to eliminate Cr(VI), while offering the advantages of reduced cost, high capacity of adsorption and respect for the environment. Therefore, it could be a promising adsorbent in environmental applications.

Acknowledgment

The authors gratefully acknowledge financial support from the Centre National de la Recherche Scientifique (CNRS), the MESRS-Algeria, the University of Lille and the Hauts-de-France region.

References

Alizadeh, A., Abdi, G., Khodaei, M.M., Ashokkumar, M., Amirian, J., 2017. Graphene oxide/Fe_3O_4/SO_3H nanohybrid: a new adsorbent for adsorption and reduction of Cr(VI) from aqueous solutions. RSC Adv. 7, 14876.

Ayawei, N., Ebelegi, A.N., Wankasi, D., 2017. Modelling and interpretation of adsorption isotherms. J. Chem. 2017, 3039817.

Azizian, S., 2004. Kinetic models of sorption: a theoretical analysis. J. Colloid Interface Sci. 276, 47-52.

Azizian, S., Eris, S., Wilson, L.D., 2018. Re-evaluation of the century-old Langmuir isotherm for modeling adsorption phenomena in solution. Chem. Phys. 513, 99-104.

Barnhart, J., 1997. Occurrences, Uses, and Properties of Chromium. Regulatory Toxicol. Pharm. 26, S3-S7.

Budimir, M., Jijie, R., Ye, R., Barras, A., Melinte, S., Silhanek, A., Markovic, Z., Szunerits, S., Boukherroub, R., 2019. Efficient capture and photothermal ablation of planktonic bacteria and biofilms using reduced graphene oxide-polyethyleneimine flexible nanoheaters. J. Mater. Chem. B 7, 2771-2781.

636 Curtis, K.A., Miller, D., Millard, P., Basu, S., Horkay, F., Chandran, P.L., 2016. Unusual salt
637 and pH induced changes in polyethylenimine solutions. Plos One 11, e0158147.
638 Dai, J., Ren, F., Tao, C.Y., 2012. Adsorption of Cr(VI) and speciation of Cr(VI) and Cr(III) in
639 aqueous solutions using chemically modified chitosan. Int. J. Environ. Res. Public Health 9,
640 1757-1770.
641 Darabi, S.F.S., Bahramifar, N., Khalilzade, M.A., 2018. Equilibrium, thermodynamic and
642 kinetics studies on adsorption of eosin Y and red X-GRL from aqueous solution by treated
643 rice husk. J. Appl. Res. Water Wastewater 9, 392-398.
644 Deng, S., Ting, Y.P., 2005. Polyethylenimine-modified fungal biomass as a high-capacity
645 biosorbent for Cr(VI) anions: Sorption capacity and uptake mechanisms. Environm. Sci.
646 Technol. 39, 8490–8496.
647 El Ouardi, M., Laabd, M., Abou Oualid, H., Brahmi, Y., Abaamrane, A., Elouahli, A., Ait
648 Addi, A., Laknifli, A., 2019. Efficient removal of p-nitrophenol from water using
649 montmorillonite clay: insights into the adsorption mechanism, process optimization, and
650 regeneration. Environ. Sci. Pollut. R 26, 19615-19631.
651 Fan, L., Luo, C., Sun, M., Qiu, H., 2012. Synthesis of graphene oxide decorated with
652 magnetic cyclodextrin for fast chromium removal. J. Mater. Chem. 22, 24577-24583.
653 Fan, X., Peng, W., Li, Y., Li, X., Wang, S., Zhang, G., Zhang, F., 2008. Deoxygenation of
654 exfoliated graphite oxide under alkaline conditions: A green route to graphene preparation.
655 Adv. Mater. 20, 4490-4493.
656 Fang, Y., Lv, Y., Che, R., Wu, H., Zhang, X., Gu, D., Zheng, G., Zhao, D., 2013. Two-
657 dimensional mesoporous carbon nanosheets and their derived graphene nanosheets: Synthesis
658 and efficient lithium ion storage. J. Am. Chem. Soc. 135, 1524-1530.

659 Fellahi, O., Das, M.R., Coffinier, Y., Szunerits, S., Hadjersi, T., Maamache, M.,
660 Boukherroub, R., 2011. Silicon nanowire arrays-induced graphene oxide reduction under UV
661 irradiation. Nanoscale 3, 4662-4669.
662 Feng, G., Cheng, P., Yan, W., Boronat, M., Li, X., Su, J.H., Wang, J., Li, Y., Corma, A., Xu,
663 R., Yu, J., 2016. Accelerated crystallization of zeolites via hydroxyl free radicals. Science
664 351, 1188-1191.
665 Ferrandon, O., Bouabane, H., Mazet, M., 1995. Tests for the validity of different models used
666 for the adsorption of sSolutes on activated carbon. J. Water Sci. 8, 183-200.
667 Foo, K.Y., Hameed, B.H., 2010. Insights into the modeling of adsorption isotherm systems.
668 Chem. Eng. J. 156, 2-10.
669 Freundlich, H.M.F., 1906. Over the adsorption in solution. Z. Phys. Chem. 57, 385-470.
670 Ge, H.C., Ma, Z.W., 2015. Microwave preparation of triethylenetetramine modified graphene
671 oxide/chitosan composite for adsorption of Cr(VI). Carbohydr. Polym. 131, 280-287.
672 Hayes, W.I., Joseph, P., Mughal, M.Z., Papakonstantinou, P., 2014. Production of reduced
673 graphene oxide via hydrothermal reduction in an aqueous sulphuric acid suspension and its
674 electrochemical behaviour. J. Solid State Electrochem. 19, 361-380.
675 He, C., Yang, Z.Q., Ding, J., Chen, Y.C., Tong, X.W., Li, Y., 2017. Effective removal of
676 Cr(VI) from aqueous solution by 3-aminopropyltriethoxysilane-functionalized graphene
677 oxide. Colloids Surf. A 520, 448-458.
678 Ho, Y.S., Mckay, G., 1999. Comparitive sorption kinetic studies of dye and aromatic
679 compounds onto fly ash. J. Environ. Sci. Health. A 34, 1179-1204.
680 Ho, Y.S., Porter, J.F., McKay, G., 2002. Equilibrium isotherm studies for the sorption of
681 divalent metal ions onto peat: copper, nickel and lead single component systems. Water, Air,
682 Soil Pollution 141, 1-33.

683 Huang, H.H., Kanishka, K., De Silva, H., Kumara, G.R.A., Yoshimura, M., 2018. Structural
684 evolution of hydrothermally derived reduced graphene oxide. Sci. Rep. 8, 6849.
685 Jabeen, H., Chandra, V., Jung, S., Lee, J.W., Kim, K.S., Kim, S.B., 2011. Enhanced Cr(VI)
686 removal using iron nanoparticle decorated graphene. Nanoscale 3, 3583–3585.
687 Langmuir, I., 1918. The adsorption of gases on plane surface of glass, mica and platinum. J.
688 Am. Chem. Soc. 40, 1361-1403.
689 Li, S., Kang, E.T., Neoh, k.G., Ma, Z.H., Tan, K.L., Huang, W., 2001. *In situ* XPS studies of
690 thermally deposited potassium on poly(p-phenylene vinylene) and its ring-subtituted
691 derivatives. Appl. Surf. Sci. 181, 201-210.
692 Liu, B., Huang, Y., 2011. Polyethyleneimine modified eggshell membrane as a novel
693 biosorbent for adsorption and detoxification of Cr(VI) from water. J. Mater. Chem. 21, 17413.
694 Liu, H., Kuila, T., Kim, N.H., Ku, B.-C., Lee, J.H., 2013. In situ synthesis of the reduced
695 graphene oxide-polyethyleneimine composite and its gas barrier properties. J. Mater. Chem. A
696 1, 3739-3746.
697 Lu, N., Wang, J., Floresca, H.C., Kim, M.J., 2012. In situ studies on the shrinkage and
698 expansion of graphene nanopores under electron beam irradiation at temperatures in the range
699 of 400-1200°C. Carbon 50, 2961-2965.
700 Luo, T., Tian, X., Yang, C., Luo, W., Nie, Y., Wang, Y., 2017. Polyethylenimine-
701 functionalized corn bract, an agricultural waste material, for efficient removal and recovery of
702 Cr(VI) from aqueous solution. J. Agr. Food Chem. 65, 7153-7158.
703 Ma, H.L., Zhang, Y., Hu, Q.H., Yan, D., Yu, Z.Z., Zhai, M., 2012. Chemical reduction and
704 removal of Cr(VI) from acidic aqueous solution by ethylenediamine-reduced graphene oxide.
705 J. Mater. Chem. 22, 5914.

706 Nasrollahpour, A., Moradi, S.E., Khodaveisi, J., 2017. Effective removal of hexavalent
707 chromium from aqueous solutions using ionic liquid modified graphene oxide sorbent. Chem.
708 Biochem. Eng. Q. 31, 325-334.
709 Nezar, S., Cherifi, Y., Barras, A., Addad, A., Dogheche, E., Saoula, N., Laoufi, N.A.,
710 Szunerits, S., Boukherroub, R., 2019. Efficient reduction of Cr(VI) to Cr(III) under visible
711 light irradiation using CuS nanostructures. Arabian J. Chem. 12, 215-224.
712 Nia, Z.K., Chen, J.Y., Tang, B., Yuan, B., Wang, X.G., Li, J.L., 2017. Optimizing the free
713 radical content of graphene oxide by controlling its reduction. Carbon 116, 703-712.
714 Pakulski, D., Czepa, W., Witomska, S., Aliprandi, A., Pawluć, P., Patroniak, V., Ciesielski,
715 A., Samori, P., 2018. Graphene oxide-branched polyethylenimine foams for efficient removal
716 of toxic cations from water. J. Mater. Chem. A 6, 9384-9390.
717 Ramanathan, T., Fisher, F.T., Ruoff, R.S., Brinson, L.C., 2005. Amino-functionalized carbon
718 nanotubes for binding to polymers and biological systems. Chem. Mater. 17, 1290-1295.
719 Sahni, M., Locke, B.R., 2006. Quantification of hydroxyl radicals produced in aqueous phase
720 pulsed electrical discharge reactors. Ind. Eng. Chem. Res. 45, 5819-5825.
721 Sandhya, B., Tonni, A.K., 2004. Cr(VI) removal from synthetic wastewater using coconut
722 shell charcoal and commercial activated carbon modified with oxidizing agents and/or
723 chitosan. Chemosphere 54, 951–967.
724 Shao, L., Li, J., Guang, Y., Zhang, Y., Zhang, H., Che, X., Wang, Y., 2016.
725 PVA/polyethyleneimine-functionalized graphene composites with optimized properties.
726 Mater. Design 99, 235-242.
727 Singh, S.K., Dhavale, V.M., Boukherroub, R., Kurungot, S., Szunerits, S., 2017. N-doped
728 Porous Reduced Graphene Oxide as an Efficient Electrode Material for High Performance
729 Flexible Solid-state Supercapacitor. Appl. Mater. Today 8, 141-149.

730 Sun, Y., Li, C., Shi, G., 2012. Nanoporous nitrogen doped carbon modified graphene as
731 electrocatalyst for oxygen reduction reaction. J. Mater. Chem. 22, 12810-12816.
732 Temkin, M.I., 1941. Adsorption equilibrium and the kinetics of processes on
733 nonhomogeneous surfaces and in the interaction between adsorbed molecules. Zh. Fiz. Chim.
734 15, 296-332.
735 Tong, W., Zhang, Y., Zhang, Q., Luan, X., Duan, Y., Pan, S., Lv, F., An, Q., 2015. Achieving
736 significantly enhanced dielectric performance of reduced graphene oxide/polymer composite
737 by covalent modification of graphene oxide surface. Carbon 94, 590-598.
738 Wang, D., Zhang, G., Zhou, L., Wang, M., Cai, D., Wu, Z., 2017. Synthesis of a
739 multifunctional graphene oxide-based magnetic nanocomposite for efficient removal of
740 Cr(VI). Langmuir 33, 7007–7014.
741 Wu, T.N., Shi, M.C., 2010. pH-affecting sonochemical formation of hydroxyl radicals under
742 20 KHz ultrasonic irradiation. Sustain. Environ. Res. 20, 245-250.
743 York, S.S., Boesch, S.E., Wheeler, R.A., Frech, R., 2003. Vibrational assignments for high
744 molecular weight linear polyethylenimine (LPEI) based on monomeric and tetrameric model
745 compounds. Macromolecules 36, 7348-7351.
746 Yuan, X., Wang, Y., Wang, J., Zhou, C., Tang, Q., Rao, X., 2013. Calcined graphene/MgAl
747 layered double hydroxides for enhanced Cr(VI) removal. Chem. Eng. J. 221, 204-213.
748 Zhang, X., Zhang, L., Li, A., 2018a. Eucalyptus sawdust derived biochar generated by
749 combining the hydrothermal carbonization and low concentration KOH modification for
750 hexavalent chromium removal. J. Environm. Management 206, 989-998.
751 Zhang, Y., Ma, H.L., Peng, J., Zhai, M., Yu, Z.Z., 2013. Cr(VI) removal from aqueous
752 solution using chemically reduced and functionalized graphene oxide. J. Mater. Sci. 48, 1883-
753 1889.

754 Zhang, Z., Gao, T., Si, S., Liu, Q., Wu, Y., Zhou, G., 2018b. One-pot preparation of P(TA
755 TEPA)-PAM-RGO ternary composite for high efficient Cr(VI) removal from aqueous
756 solution. Chem. Eng. J. 343, 207-216.
757 Zhang, Z., Luo, H., Jiang, X., Jiang, Z., Yang, C., 2015. Synthesis of reduced graphene oxide-
758 montmorillonite nanocomposite and its application in hexavalent chromium removal from
759 aqueous solutions. RSC Adv. 5, 47408-47417.
760 Zhao, D.L., Gao, X., Wu, C.N., Xie, R., Feng, S.J., Chen, C.L., 2016. Facile preparation of
761 amino functionalized graphene oxide decorated with Fe_3O_4 nanoparticles for the adsorption of
762 Cr(VI). Appl. Surf. Sci. 384, 1-9.
763 Zhao, H., Wang, J., Zhang, D., Dai, Q., Han, Q., Du, P., Liu, C., Xie, Y., Zhang, Y., Cao, H.,
764 Fan, Z., 2017. Chloro-benquinone modified on graphene oxide as metal-free catalyst: Strong
765 promotion of hydroxyl radical and generation of ultra-small graphene oxide. Sci. Rep. 7,
766 42643.
767 Zhou, J., Wang, Y., Wang, J., Qiao, W., Long, D., Ling, L., 2016. Effective removal of
768 hexavalent chromium from aqueous solutions by adsorption on mesoporous carbon
769 microspheres. J. Colloid Interface Sci. 462, 200-207.
770